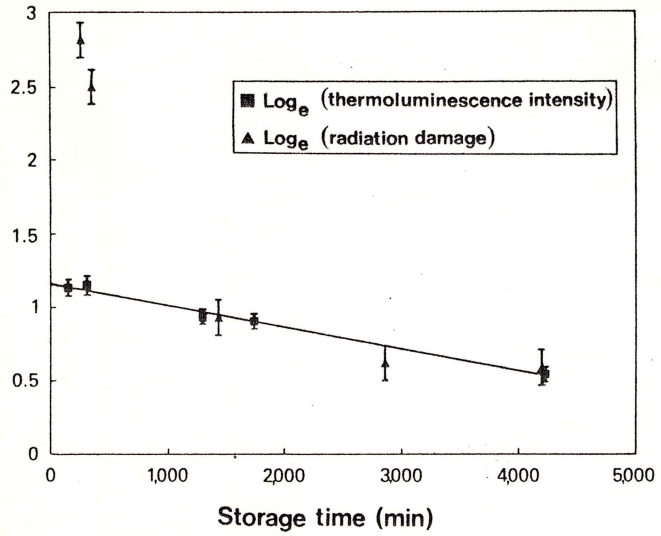

Fig. 4 Decrease in the thermoluminescence intensity of the 115 °C peak and decrease of radiation damage (reduction in scintillation output) for samples stored at 22 °C following a 30-min ultraviolet exposure.

normally involved in the scintillation process, then the scintillation output will be reduced in proportion to the fraction of these electrons that become trapped and the filling of these metastable energy levels will be similar to the mechanism which stores thermoluminescence. Thus, we looked for correlations between the thermoluminescence traps and the traps responsible for radiation damage, first by comparing the behaviour of thermoluminescence and radiation damage as a function of radiation exposure. Figure 3 shows the intensity of the 115 °C peak as a function of ultraviolet irradiation time and also the radiation damage induced in the 6 mm × 24 mm sample by the same exposure, defined as the reduction in the scintillation response to 662-keV γ rays following the ultraviolet exposure. Although the error bars are large, the radiation damage appears to follow about the same pattern as the thermoluminescence, saturating after about the same exposure, except that the radiation damage is larger than the thermoluminescence for short exposures, suggesting a contribution from an additional trapping centre.

We compare also the decay of the thermoluminescence to annealing of radiation damage in BGO. Scintillation efficiency, reduced by ultraviolet, γ or sunlight exposure, will recover subsequently if the crystal is stored at room temperature for several days, or at an elevated temperature for a shorter time, which is similar to the decay of thermoluminescence. Thus a second technique was used to investigate the possible connection between thermoluminescence and radiation damage. Both the thermoluminescence sample and the scintillator sample were irradiated with ultraviolet for 30 min, which resulted in a 11% decrease in the scintillation efficiency (light output) and also stored a thermoluminescence signal. The samples were stored at room temperature and the scintillation efficiency and thermoluminescence intensity of the 115 °C peak were measured as a function of time. Figure 4 shows the decay of the thermoluminescence signal and the simultaneous recovery of the scintillation efficiency (plotted as the decrease in radiation damage), which, for times greater than 1,000 min, occur at the same rate, again suggesting a correlation between these phenomena. But for shorter times the radiation damage decreases more rapidly, probably owing to the depopulation of a shallower trap, perhaps the one observed at 65 °C; preliminary measurements of the radiation-damage decay time of a sample stored at 10 °C, together with the data in Fig. 4, suggest a depth of approximately 0.9 eV for the shallow trap, which is approximately the depth expected for the 65 °C peak, although it was not possible to determine it directly by thermoluminescence measurements. Thus, the population of this shallow trap is probably related to the short term recovery of radiation damage, whereas the population of the 1.1 eV trap (115 °C peak) is related to the longer term recovery of radiation damage.

Two conclusions may be drawn from these initial results. First, BGO displays a relatively-strong thermoluminescence signal with reasonably well-defined peaks. The 115 °C peak readily lends itself to a detailed investigation of decay time, trap depth and frequency factor, but the other peaks will require thermal or optical bleaching or perhaps slower heating rates to isolate them for further study. Second, the measurements reported here suggest that the thermoluminescence traps and the radiation damage traps may be related. In particular, both thermoluminescence and radiation damage (that is, reduced scintillation efficiency) are produced by the same type and intensity of excitation (ultraviolet, γ and sunlight), both quantities increase with increasing ultraviolet exposure and saturate after similar exposures and both quantities decay at the same rate following excitation, which suggests that the thermoluminescence traps and the radiation damage traps are indeed related and may in fact be the same traps. If this is indeed true, then thermoluminescence could prove to be a valuable tool for studying both the radiation damage mechanism and the basic scintillation mechanism itself, the main advantage being its high sensitivity. Further investigation of the correlation between the 65 °C peak and short-term radiation-damage recovery and comparison of thermoluminescence properties with trace element compositions of different BGO crystals should provide further insight into the relationship between these effects in BGO.

I thank W. A. Loomis and J. S. Schweitzer for helpful discussions.

Received 10 September; accepted 26 November 1984.

1. Bakken, J., Isaila, M., Piroue, P., Stickland, D. & Sumner, R. *IEEE Trans. Nucl. Sci.* **31**, 180–183 (1984).
2. Cho, S. H. & Farukhi, M. R. *J. nucl. Med.* **18**, 840–851 (1977).
3. Schweitzer, J. S. *Proc. Int. Workshop Bismuth Germanate* Physics Dep. Rep., 696–697 (Princeton University, 1982).
4. Bobbink, G. J. *et al.* SLAC-PUB-3339, *3rd Int. Conf. Instrumentation Colliding Beam Physics* (Novosibirsk, USSR, 1984).
5. Horowitz, Y. S. *Thermoluminescence and Thermoluminescent Dosimetry* (CRC, Boca Raton, Florida, 1984).
6. Birks, J. B. *The Theory and Practice of Scintillation Counting* (Pergamon, Oxford, 1964).
7. Maccio-Serpia, P., Rucci, A. & Serpi, A. *J. Luminescence* **9**, 488–501 (1975).

Dirty snow after nuclear war

Stephen G. Warren* & Warren J. Wiscombe†

* Department of Atmospheric Sciences, AK-40, University of Washington, Seattle, Washington 98195, USA
† NASA-Goddard Space Flight Center, Greenbelt, Maryland 20771, USA

The notion that smoke from fires started by nuclear explosions could alter the Earth's climate[1] is supported by quantitative models of climate[2–5,27] showing that severe cooling may be expected at continental surfaces in the first few months following a full-scale nuclear war, because of the reduced transmission of sunlight through the atmospheric smoke. Whether or not these model results are correct, we show here that the smoke could continue to cause significant climatic disruption even after it has fallen from the atmosphere, by lowering the reflectivity of snow and sea-ice surfaces, with possible effects on climate in northern latitudes caused by enhanced absorption of sunlight. Indeed, on Arctic sea ice and on the ablation area of the Greenland ice sheet, the reduced reflectivity could persist for several years.

The fraction of light reflected by pure snow is >90% at visible wavelengths, but much lower in the near-infrared. The spectral measurements can essentially be explained by radiative-transfer modelling[6]. As convective and latent-heat transfers over snowpacks are, typically, smaller than the radiative fluxes[7], the

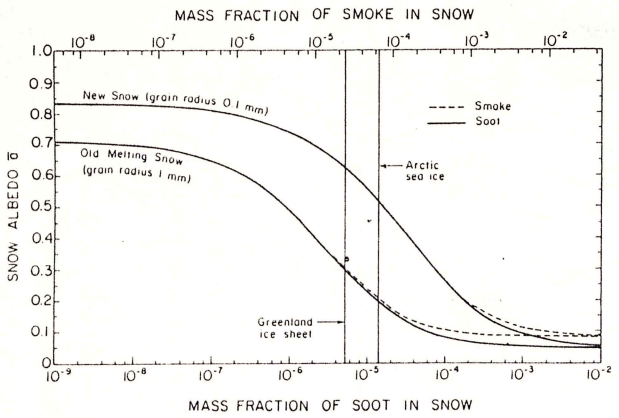

Fig. 1 Spectrally-averaged snow albedo as a function of soot (bottom scale) or smoke (top scale) content, for two different snow grain sizes. (The grain size is the radius of an optically-'equivalent' sphere and is related to the volume/surface ratio of nonspherical snow grains[11].) The spectral complex refractive index of ice is obtained from ref. 24. 'Soot' is assumed to have complex refractive index $1.8-0.5i$, independent of wavelength, and density 1.0 g cm^{-3} (footnote 3 of ref. 9) and to be present as uniform spheres of radius 0.1 μm. These values imply a mass absorption coefficient for soot decreasing with wavelength from 11.7 m^2 g^{-1} at $\lambda = 300$ nm to 4.6 m^2 g^{-1} at $\lambda = 1{,}000$ nm. 'Smoke' also has density 1.0 g cm^{-3}; its refractive index, $1.55-0.1i$, was specified by NAS[14] for visible wavelengths, but is also used here for the near-infrared. This assumption is not crucial, because the major reduction of albedo is at visible wavelengths; pure snow already has low albedo in the near-infrared because of the greater absorptivity of ice there. The smoke has log-normal size distribution with number-mode radius $r_m = 0.1$ μm and log-normal width $\gamma = 2.0$ (Table 5.7 of ref. 14). This distribution has effective radius[25] $r_{eff} = 0.33$ μm. Doubling the mode radius to $r_m = 0.2$ μm ($r_{eff} = 0.66$ μm), to simulate possible aggregation of the smoke particles, would have the same effect as reducing the concentration of smoke in snow by a factor of 1.5. Calculation is for an 'external mixture' of soot particles and ice particles; for an internal mixture the curves should be shifted by a factor of ~2 to the left. The incident solar radiation spectrum is assumed to be that for subarctic summer, clear sky, solar zenith angle 53°, at sea level. A given concentration of impurities would reduce albedo somewhat more under a cloudy sky. Vertical lines give concentrations for the scenarios discussed in the text, for smoke distributed through one month's snowfall.

energy budget of the snowpack is strongly influenced by the spectrally-averaged albedo

$$\bar{a} = \frac{\int_0^\infty a(\lambda)S(\lambda)\,d\lambda}{\int_0^\infty S(\lambda)\,d\lambda} \qquad (1)$$

where $a(\lambda)$ is the snow albedo (ratio of upward to downward radiation flux) at wavelength λ and $S(\lambda)$ is the spectral distribution of solar energy flux incident on the surface (W m^{-2} μm^{-1}). Pure snow reflects 70–85% of the solar energy incident on it, depending primarily on the snow grain size which normally grows as the snow ages[8]; $\bar{a}$ is 80–85% for new snow of grain radius r in the range 50–100 μm and $\bar{a} \simeq 70\%$ for old melting snow ($r \simeq 1$ mm). The albedo is also influenced by solar zenith angle and by cloud cover.

Small amounts of absorptive impurities in snow can reduce the albedo dramatically in spectral regions where it is high (visible wavelengths). We previously computed[9] the radiative effects of graphitic carbon, 'soot' (mass fraction $\leq 10^{-7}$) distributed uniformly through a snowpack, and subsequent experiments, measuring both albedo and soot content[10], agreed within the experimental uncertainty (a factor of ~2 in soot content) with predictions of our radiation model[11].

For the present purpose, the earlier results (Fig. 7 and footnote 3 of ref. 9) must be extended to larger amounts of soot and also be averaged over wave-length. The solar spectrum at the Earth's surface, $S(\lambda)$, is obtained using Wiscombe's atmospheric radiation model[12] for the subarctic-summer standard atmosphere[13]. Figure 1 shows the dependence of snow albedo on soot content, for two values of snow grain size. A given amount of soot causes a greater reduction in albedo in old snow than in new snow because the radiation penetrates deeper on average in old coarse-grained snow and therefore encounters more absorbing material before being scattered back out of the snowpack.

Results are also shown of calculations using the optical properties of the 'smoke' for the baseline nuclear war scenario of the US National Academy of Sciences (NAS)[14]. As this smoke contains 20% soot and 80% transparent oily compounds, it is less absorptive than pure soot, but the effects of a given amount of 'smoke' on snow albedo closely match those calculated for pure soot of the amount present in the smoke. Thus, in Fig. 1, by shifting the top scale (for smoke) by a factor of ~5 relative to the bottom scale (for soot), we were able to superimpose the results for 'smoke' on those for 'soot', except in very polluted snow (dashed curves).

All these calculations are done by modelling soot or smoke in snow as an 'external mixture' (impurity particles separated from ice particles), which may underestimate the true effect of the impurities as a given reduction of albedo can be achieved by about half as much soot, if the soot is instead located inside the ice grains[15,16] ('internal mixture'). (However, the snow albedos, $\bar{a}$, of Chylek *et al.*[15], are too low because, for $S(\lambda)$ in equation (1), these workers used the solar spectrum at the top of the atmosphere instead of at the snow surface; for example, the absorptivity of pure snow with $r = 0.1$ mm should be 0.17 (Fig. 1 here) instead of 0.21 in their Fig. 7.) The most probable situation, in which smoke is scavenged by falling snow crystals, ending up on the surface of the ice grains[17], would probably give results intermediate between those of external and internal mixtures.

We now use Fig. 1 to estimate the reduction of snow albedo following nuclear war for the case of snow covering the sea ice of the Arctic Ocean, the surrounding tundra of the northern continents and the Greenland ice sheet, areas where the absorption of sunlight would be most enhanced because the effect of changing snow albedo is not muted by forest cover. We use the NAS[14] baseline scenario in which 1.8×10^{14} g of smoke is injected into the atmosphere. Because of its proximity to sources of smoke, the Arctic may suffer more pollution than the average for the Northern Hemisphere, but here we simply assume the smoke is uniformly deposited over the Northern Hemisphere, so the total smoke fallout is 0.71 g m^{-2}. The e-folding decay time for smoke fallout is probably in the range 10–30 days. (For the baseline scenario in Fig. 1 of ref. 2 it is 30 days.) Using an average precipitation of 13 g cm^{-2} yr^{-1} for the Arctic Ocean[18] and 37 g cm^{-2} yr^{-1} for Greenland[19], the mass fraction of smoke in the snow would be 6.5×10^{-5} on the Arctic sea ice and 2.2×10^{-5} on Greenland, if distributed through one month's precipitation in each case. These concentrations are indicated by vertical lines in Fig. 1. The values of $\bar{a}$ intersected by these lines indicate that the fraction of solar energy absorbed by snow ($1-\bar{a}$) on the Arctic Ocean would increase by a factor of 2.8 (new snow)–2.7 (old melting snow) and on Greenland by a factor of 2.2–2.4, respectively. But a net positive effect on the snow energy budget cannot be expected until most of the soot has fallen from the atmosphere so that it no longer blocks the sunlight.

The estimates of smoke concentration in the snow depend, of course, on the snowfall rate and the smoke sedimentation rate and on the total smoke injection into the atmosphere, all of which are highly uncertain. The snowfall rate may be reduced, for example, because of the greater atmospheric stability in the presence of smoke[2]. The vertical lines in Fig. 1, therefore, are only illustrative of the possible magnitude of the effect and are not meant to be quantitative predictions. Other scenarios for different amounts of smoke can be read off Fig. 1, as desired. For example, if the total amount of smoke were the same as we assumed, but fell over a period of two months instead of one

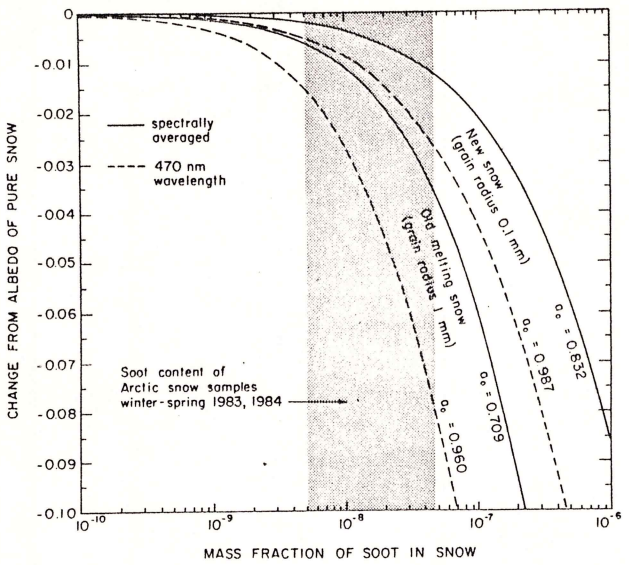

Fig. 2 Computed effects on snow albedo caused by small mass fractions of soot. Soot size distribution and refractive index, snow grain sizes and solar radiation spectrum are the same as used in Fig. 1. The changes from the albedo values of pure snow, a_0, are plotted; the spectrally-averaged changes (solid lines) correspond to the left-most portion of the plots in Fig. 1, on an expanded vertical scale here. The dashed lines are calcuations at the wavelength where snow albedo is most sensitive to soot content ($\lambda = 470$ nm). The reduction in spectrally-averaged albedo is thus approximately half that at visible wavelengths. The shaded region indicates the range of soot concentrations determined[26] in 12 samples of snowfall collected from Arctic Canada, Alaska, Greenland and Svalbard during winter and spring 1983–84. To ensure consistency between soot measurement and albedo calculation, they have been multiplied here by the factor 0.85; previously[26], a mass absorption coefficient $k_{abs} = 8.5\ m^2\ g^{-1}$ for ambient soot at $\lambda = 525$ nm was assumed, whereas the Mie calculation for the soot parameters used here gave $k_{abs} = 10.0\ m^2\ g^{-1}$.

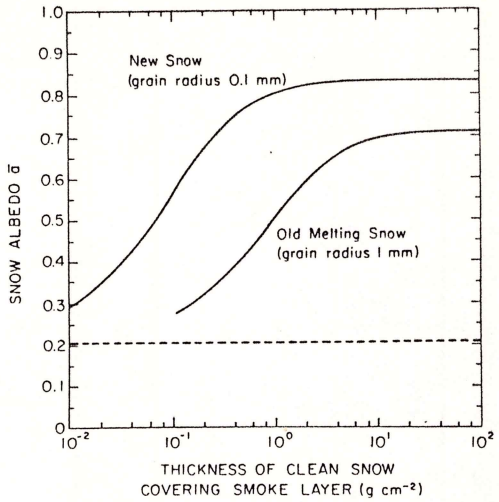

Fig. 3 Spectrally-averaged snow albedo as a function of the thickness of clean snow covering the smoke layer, for two different snow grain sizes. The smoke is assumed to be distributed through a layer of coarse-grained snow, $r = 1$ mm, corresponding to one month's snowfall in the Arctic Ocean, so that it has spectrally-averaged albedo 0.203 when on the surface (intersection of vertical line 'Arctic sea ice' with dashed curve in Fig. 1, shown here as horizontal dashed line). Solar radiation spectrum is the same as for Fig. 1. No calculations are done for snowpack thicknesses less than a monolayer of snow grains.

(or if it fell quickly, but was distributed through two months snowfall by wind-drifting), the vertical lines should be moved a factor of two to the left, changing the albedo of polluted new snow on Arctic sea ice from 0.52 to 0.60; of old snow from 0.20 to 0.27.

These hypothetical effects of nuclear war are all much larger than the possible reduction of snow albedo of a few per cent caused by the small concentrations of soot found at present in Arctic snow (Fig. 2).

In the above four cases (intersections of lines in Fig. 1), the polluted layer has sufficient optical thickness for the albedo to be unaffected by the presence of clean snow beneath. However, light penetrates clean snow more deeply than polluted snow. Figure 3 shows how the albedo recovers to high values as the smoke layer is covered by clean snow, assuming for the smoke layer the lowest albedo of the four cases, $\bar{a} = 0.203$. The thickness of clean snow necessary to hide the smoke layer, such that the smoke retains only a 1% effect on $\bar{a}$, is 2 g cm^{-2} for new snow and 10 g cm^{-2} for old melting snow (corresponding to about 2 and 10 months precipitation in the Arctic, respectively); this means, of course, that as the clean snow ages, its hiding power diminishes.

Although the albedo would rise as clean snowfalls bury the smoke, the polluted layer may be exposed again during a subsequent melt-season and so hasten the disappearance of the snow from the Arctic tundra and sea ice. Experiments are needed to determine whether small smoke particles tend to concentrate at the surface of melting snow, as do micrometre-size dust particles[20].

At high altitude locations on the Greenland ice sheet, the incident solar spectrum $S(\lambda)$ is somewhat different from that used here (compare Fig. 1 caption) but, judging from high-altitude Antarctic calculations[21], the difference in $\bar{a}$ is small enough for these figures still to be used. Unlike the Antarctic ice sheet, where temperatures remain far below freezing throughout the year, in Greenland there is normally some melting in summer over 70% of the ice sheet[19,22]. This melting could be enhanced by smoke fallout, especially in the ablation area of the Greenland ice sheet (~15% of the ice sheet area) where the smoke would be exposed repeatedly in subsequent summers. The effect on the mass budget of Greenland may be estimated from Ambach's model[23].

Persistent consequences would also be expected on multi-year Arctic sea ice. Because the snow now melts completely every summer on Arctic sea ice and because of the direction of sea-ice growth (by freezing at the bottom), the smoke layer would probably be uncovered repeatedly in subsequent summers to darken the ice.

We thank John Birks, Stephen Schneider and Conway Leovy for encouraging us to do these calculations; Jerry Mahlman for information on smoke lifetime and transport in the atmosphere; Antony Clarke for pre-publication data on soot in Arctic snow; and Walter Ambach, Carl Benson, Arnold Hanson and Starley Thompson for advice. Our research on optical properties of snow and ice is supported by NSF grant ATM-83-15337. The computations were done at the National Center for Atmospheric Research.

Received 11 June; accepted 23 November 1984.

1. Crutzen, P. J. & Birks, J. W. *Ambio* **11**, 114–125 (1982).
2. Turco, R. P., Toon, O. B., Ackerman, T. P., Pollack, J. B. & Sagan, C. *Science* **222**, 1283–1292 (1983).
3. Covey, C., Schneider, S. H. & Thompson, S. L. *Nature* **308**, 21–25 (1984).
4. Thompson, S. L. *et al. Ambio* **13**, 236–243 (1984).
5. Crutzen, P. J., Brühl, C. & Galbally, I. E. *Climatic Change* **6**, 323–364 (1984).
6. Wiscombe, W. J. & Warren, S. G. *J. atmos. Sci.* **37**, 2712–2733 (1980).
7. Paterson, W. S. B. *The Physics of Glaciers* 2nd edn, Ch. 14 (Pergamon, Oxford, 1981).
8. LaChapelle, E. R. *Field Guide to Snow Crystals*, 60–74 (University of Washington Press, 1969).
9. Warren, S. G. & Wiscombe, W. J. *J. atmos. Sci.* **37**, 2734–2745 (1980).
10. Grenfell, T. C., Perovich, D. K. & Ogren, J. A. *Cold Regions Sci. Technol.* **4**, 121–127 (1981).
11. Warren, S. G. *Rev. Geophys. Space Phys.* **20**, 67–89 (1982).
12. Wiscombe, W. J., Welch, R. & Hall, W. *J. atmos. Sci.* **41**, 1336–1355 (1984).
13. McClatchey, R. A., Fenn, R. W., Selby, J. E. A., Volz, F. E. & Garing, J. S. *Optical Properties of the Atmosphere* 3rd edn (AFCRL-72-0497, Air Force Geophysics Laboratory, Hanscom AFB, Massachusetts, 1972).
14. National Academy of Sciences *Report of the Committee on Atmospheric Effects of Nuclear Explosions* (Washington, DC, in the press).
15. Chylek, P., Ramaswamy, V. & Srivastava, V. *J. geophys. Res.* **88**, 10837–10843 (1983).
16. Bohren, C. F. & Hoffman, D. R. *Absorption and Scattering of Light by Small Particles*, 446 (Wiley-Interscience, New York, 1983).
17. Prodi, F. in *Preprints International Conference on Cloud Physics*, 70–75 (American Meteorological Society, Boulder, Colorado, 1976).

18. Vowinckel, E. & Orvig, S. in *Climates of the Polar Regions* (ed. Orvig, S.) 207 (Elsevier, Amsterdam, 1970).
19. Bader, H. *The Greenland Ice Sheet* (CRREL Rep. I-B2, U.S. Army Cold Regions Research and Engineering Laboratory, Hanover, New Hampshire, 1961).
20. Higuchi, K. & Nagoshi, A. in *Isotopes and Impurities in Snow and Ice*, 95–97 (International Association of Hydrological Sciences Publ. No. 118, 1977).
21. Wiscombe, W. J. & Warren, S. G. in *International Radiation Symposium Volume of Extended Abstracts*, 380–382 (Colorado State University, Fort Collins, 1980).
22. Benson, C. S., *Stratigraphic Studies in the Snow and Firn of the Greenland Ice Sheet* (SIPRE Research Rep. 70, U.S. Army Cold Regions Research and Engineering Laboratory, Hanover, New Hampshire, 1962).
23. Ambach, W. *Ann. Glaciol.* **6** (in the press).
24. Warren, S. G. *Appl. Opt.* **23**, 1206–1225 (1984).
25. Hansen, J. E. & Travis, L. D. *Space Sci. Rev.* **16**, 527–610 (1974).
26. Clarke, A. D. & Noone, K. J. *Atmos. Envir.* (in the press).
27. Robock, A. *Nature* **310**, 667–670 (1984).

Correlative 90 kyr northeast Asia–northwest Pacific climate records

Linda E. Heusser & Joseph J. Morley

Lamont-Doherty Geological Observatory of Columbia University, Palisades, New York 10964, USA

Specific regional and hemispheric responses to past variations in solar radiation demonstrate the complex interconnections that exist between components (land/sea/atmosphere) of the climate system[1,2]. Few empirical palaeoclimatic studies are available from northeastern Asia, a region essential for the construction of composite models of global climate change and critical to analyses of northwestern North American climate. Among these, Quaternary climatic data from Japan are restricted largely to pollen sequences <30 kyr BP, as limited chronostratigraphic control constrains older data[3–6]. Palaeoenvironmental studies of the northwest Pacific Ocean focus on comparing modern conditions with the last glacial maximum[7]. Continuous marine palaeoclimatic series are far from land and are not correlated directly with continental sequences[8,9]. Here we present the first continuous records of vegetation and climate from northeastern Japan over the past 90 kyr, relating them directly to sea-surface temperature (SST) estimates from the same deep-sea core, RC14-103 located in the northwest Pacific Ocean east of Hokkaido (Fig. 1). Relative stable glacial (~80–20 kyr BP) environments are cold (<4 °C) and wet (~1,000 mm), with boreal forest and tundra on Hokkaido associated with cool (<16 °C) summer and cold (<1.0 °C) winter SSTs offshore; non-glacial (~10–4 kyr BP) environments on land are warm (>8 °C) and humid (>1,200 mm), whereas SSTs are cold (10.4–14.3 °C) in summer and warm (>1.5 °C) in winter.

Modern pollen and radiolaria distributions in sediments from seas around Japan are used to interpret fossil floral and faunal changes[10,11]. Specifically, factor analysis of abundance data for 35 radiolarian species in 66 surface sediment samples from the northwest Pacific[8] yielded four assemblages accounting for 95% of the distribution variance in the data set. The four radiolarian factors correlate with surface water masses for which they are named: subtropical (Subtropic Gyre), subpolar (Subpolar Gyre), transitional (Subarctic Front) and Okhotsk (Sea of Okhotsk). Transfer functions developed from regression analyses relating these radiolarian assemblages to observed SSTs have standard errors in the estimates for winter and summer of 1.3 °C and 0.9 °C respectively. The SSTs derived from these radiolarian assemblages and vegetation/climate changes inferred from pollen assemblages in the core are correlated directly with regional and global stratigraphies[12–14]. Time control is based on radiolarian stratigraphy developed for the northwest Pacific[10]. In RC14-103, two distinct modes separated by a brief transition appear in floral and faunal down-core assemblages: (1) a postglacial mode (11 kyr BP–present), distinguished by oak-dominated broadleaf pollen and subpolar radiolarian assemblages and (2) a glacial mode (~80–18 kyr BP) characterized by spruce-dominated conifer pollen and 'Sea of Okhotsk' radiolarian assemblages (Fig. 2).

Maximum concentrations of pollen from warm temperate oak forests occurred between ~11 and 4 kyr BP, whereas spruce,

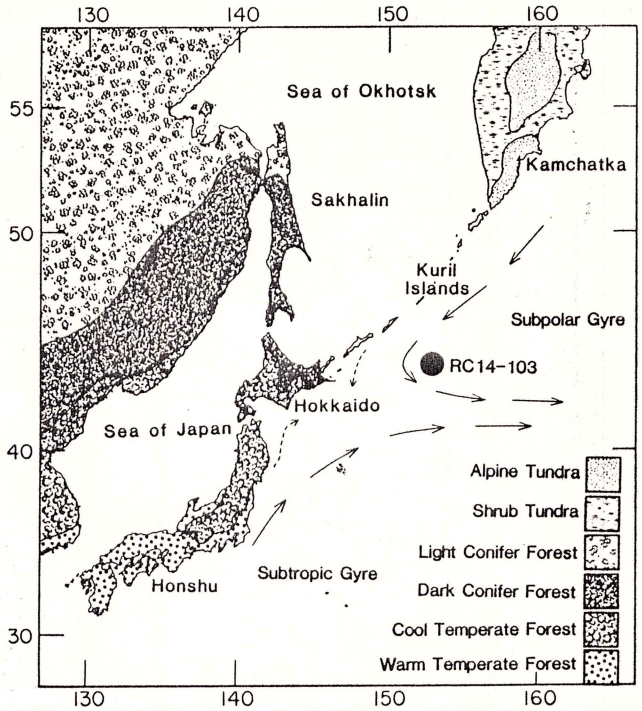

Fig. 1 Location of core RC14-103 (44°02′ N, 152°56′ E, 5,365-m water depth) in the northwest Pacific–northeast Asian study area. The core site, in the southwest portion of the Subpolar Gyre, is just north of today's Subarctic Front (confluence of currents from Subtropic and Subpolar Gyres). The flow of major surface currents in the region is indicated by arrows. Schematic vegetation distribution is modified from Tsukada[6], Walter[28] and Wang[29]. Major Japanese vegetation groups are associated closely with latitudinal and altitudinal temperature variation. Mean annual temperatures of evergreen broad-leaved (warm temperate), deciduous broad-leaved (cool temperate) and boreal/subalpine (dark) conifer forests are 13–21 °C, 6–13 °C, and <6 °C respectively[30].

hemlock (*Tsuga*), birch (*Betula*) and alder (*Alnus*) were insignificant. Climatic conditions of the youngest 4 kyr approached those of the present, with increased spruce, Japanese cedar (*Cryptomeria japonica*) and *Sphagnum* reflecting the cool moist environments of northeastern Japan. Between 18 and 11 kyr BP, birch-alder and conifer (subarctic and cold temperate) factors were prominent, with the abundance of pine and the occasional absence of Japanese cedar suggesting climates which were periodically cool and often dry[15,16]. Full glacial (25–18 kyr BP) sediments contain maximum amounts of boreal (spruce-dominated), park-tundra and tundra (including, sedge (Cyperaceae) and *Sphagnum*). High concentrations of *Selaginella selaginoides*, a common arctic and alpine tundra species[17,18], indicate that cold subarctic conditions prevailed on northern Hokkaido during this time interval. From ~60 to 25 kyr BP, slight expansion of oak and birch-alder assemblages, together with the intermittent presence of Japanese cedar, suggests there were minor variations in precipitation and temperature within an overall cold dry climate. Boreal conifers (primarily spruce), low frequency of broad-leaf taxa and a significant increase in Japanese cedar and hemlock (trees associated with cool moist environments) characterize the interval ~80–60 kyr BP. In the oldest sequence in RC14-103 (~90–80 kyr BP), pollen consists mainly of pine, oak, birch and alder, with few Japanese cedar and boreal conifers, indicating slightly warmer drier summers than in the glacial period.

Estimated SSTs vary from 3.2 °C below to 1.4 °C above present winter and 6.2 °C below and 3.0 °C above present summer temperatures (Fig. 2). The warmest Holocene SSTs are recorded for ~6–4 kyr BP. Early Holocene winter SSTs, ~1.5 °C below the present temperature, rise during the postglacial climatic optimum to values similar to the February temperature of today. Low early-Holocene summer SSTs reach a maximum at 5 kyr BP.